Proceedings of the
Annual Stability Conference
Structural Stability Research Council
Orlando, Florida, April 12-15, 2016

Automated Damage Detection and Structural Modelling with Laser Scanning

Yujie Yan[1], Burcu Guldur[2], Luke Yoder[3], Varun Kasireddy[4],
Daniel Huber[5], Sebastian Scherer[6], Burcu Akinci[7], Jerome F. Hajjar[8]

Abstract

Inspection of aging and deteriorating infrastructure such as bridges, dams, power supply infrastructures are crucial to assure their reliability as well as to estimate their remaining life. This study proposes to use small, low flying autonomous unmanned aerial vehicles, coupled with three-dimensional laser scanning, high-resolution imaging and state-of-art modeling and analysis abilities in order to provide high-precision damage detection, condition assessment and modelling of structures and infrastructure systems. In recent years, laser scanning has been shown to be effective in capturing three-dimensional geometrical information with a high degree of accuracy, which enables automatic visual damage detection and creation of high-precision information and computational models. This paper proposes a set of strategies for processing captured texture-mapped laser point cloud automatically in order to detect surface damage and large element deformation of the infrastructure system as well as to create high-fidelity computational models. Both predicted surface and determined geometric properties, which are extracted from captured texture-mapped point clouds, are used for locating, differentiating, quantifying and documenting surface damage on infrastructures. Also, high-quality volumetric finite element meshes are generated through processing the raw 3D point cloud using proposed mesh generation strategies and validated against experimental specimen. In order to show the robustness and effectiveness of these capabilities, the proposed strategies for damage detection and computational model generation are validated and tested against both synthetic and real point cloud data.

Introduction

The recent ASCE Report Card for infrastructure in the U.S. (released in July 2014) revealed that the average grade for all infrastructure types was D+, which emphasizes the importance of assessing the current conditions and performing health monitoring on infrastructure systems. Current routine inspection requires sending inspectors to observe,

[1] Graduate Research Assistant, Northeastern University, yan.yuj@husky.neu.edu
[2] Assistant Professor, Hacettepe University, burcuguldur@hacettepe.edu.tr
[3] Robotics Engineer, Robotic Institute, Carnegie Mellon University, lyoder@cmu.edu
[4] Graduate Research Assistant, Carnegie Mellon University, vkasired@andrew.cmu.edu
[5] Senior Systems Scientist, Robotic Institute, Carnegie Mellon University, huber@andrew.cmu.edu
[6] Systems Scientist, Robotic Institute, Carnegie Mellon University, basti@andrew.cmu.edu
[7] Paul Christiano Professor of Civil and Environmental Engineering, bakinci@cmu.edu
[8] CDM Smith Professor and Department Chair, Northeastern University, JF.Hajjar@neu.edu

measure and record defects manually, which is labor-intensive and dangerous. This inspection process usually requires shutting down a portion of or all of the structure's daily operation, which may result in significant inconvenience. Results recorded in this way are error-prone since they are subject to transcription errors, measurement errors, and dependence on the personal judgment of the inspector. There is also typically no automated way to compare inspection results over a period of time, so it is difficult to track the propagation of damage.

In order to assess, document, and monitor the health condition of infrastructure systems in a more rapid and practical way, in this work we are developing the use of a small, low-flying robotic assistant (i.e., an unmanned aerial vehicle), mounted with a three-dimensional laser scanner and a high-resolution camera, to capture texture-mapped laser point clouds representing the geometrical information of infrastructures. The captured texture mapped point clouds are processed later through state-of-the-art damage detection, modelling, analysis strategies. This robot provides assistance not only for routine inspection but also for the rapid assessments after disasters like earthquakes, severe storms and explosions, especially for reaching dangerous and inaccessible locations. To achieve this purpose, six main steps are proposed in this work, as shown in Fig. 1.

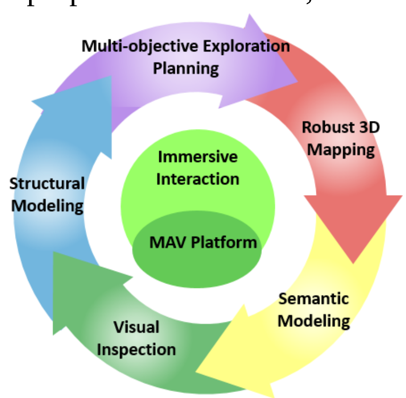

Figure 1: Research themes

Manually flying the robot in close proximity to a structure is difficult for a human pilot, and it may be difficult for a human pilot to choose a flight path from which the robot can collect complete data from the structure. Flying safely close to structures and guaranteeing complete data collection are two low-level tasks well suited for robotic algorithms (Yoder and Scherer 2015). When a human pilot is relieved of low level piloting tasks, they are free to guide the mission from a high level. In this work, an approach has been developed in which a pilot specifies the structure to be scanned by the robot using a 3D bounding box and a graphical user interface. As the robot completes the mission, the user is free to change the bounding box, or to specify new bounding boxes for the robot to perform scans. Once all surfaces are modeled inside the bounding boxes, the robot detects that the mission has been completed and returns home with high-quality data (Yoder and Scherer 2015).

Conventional terrestrial laser scanners are able to produce accurate registered point clouds because the scanner's base is stationary. In the case of an aerial laser scanner where the vehicle is moving, each measurement comes from a different aerial vehicle position. Creating a registered map in the aerial laser scanner case requires using additional sensors like inertial measurement units (IMUs) and global positioning systems (GPS). Since infrastructure inspection robots often operate in environments without sufficient GPS coverage, they must use their onboard sensors to estimate the position of the aerial vehicle. This problem is known as simultaneous localization and mapping (SLAM) since the vehicle must simultaneously estimate the aerial vehicle's position using the laser point cloud and register the point cloud using the vehicle's position. Our solution uses an IMU and a Velodyne VLP-16 laser scanner mounted on a rotating gimbal, as shown in Fig. 2(a). The IMU and laser data is processed using a novel SLAM approach to produce low latency aerial vehicle position estimates and a registered point cloud (Zhang et al. 2014).

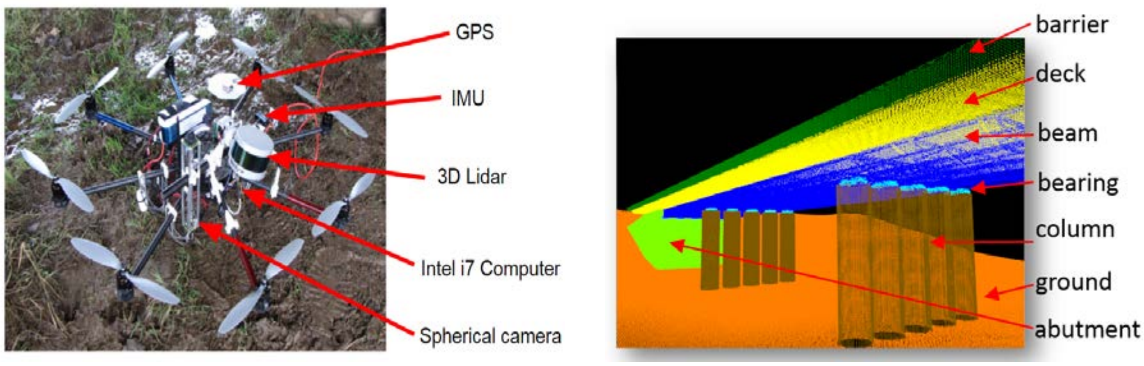

Figure 2: (a) Low-flying robots; (b) Automatic segmentation and semantic modelling

Registered point clouds provide several capabilities such as distance measurement and coarse visualization. However, in order to gain full benefit of the 3D data, we propose using semantic modeling algorithms to transform the point cloud into an information-rich, object-oriented representation – the infrastructure equivalent of a Building Information Model (BIM). Such a representation enables an inspector to interact with the robot at the symbolic level, for example by commanding the robot to inspect a bridge's columns at a 2 cm resolution and provide a report rather than having to specify each column's location and extent manually. Furthermore, the representation can provide a pathway to create computational models needed for structural assessment. Our approach uses computer vision techniques to segment components of the structure, identify the coarse topology, and recognize and model individual elements, such as columns, beams, truss structures, and abutments on a bridge as shown in Fig. 2(b) (Song, 2015 and Li, 2015).

Once the components of a structure are segmented, it is possible to determine the surface damage by using the captured texture-mapped point cloud. Both 3D point data and color information associated with each 3D point in the registered cloud are used for locating, differentiating, quantifying and documenting several damage types that include small deformations (cracks, spalling, etc.), large deformations with no change in topology (cross-sections of the components remain nearly intact) and large deformations with localized change in topology (localized cross-sectional changes where the alignments of the components are not effected entirely). The extracted surface properties along with the geometric properties of the investigated components are used for capturing the deviations from the initial conditions. These detected deviations are recorded and certain visual inspection criteria is used for assigning a condition rating to the components of the investigated structures. This process is then followed by the finite element model generation by using the components extracted from the captured point cloud to perform a detailed assessment of the current condition of the structure (Guldur, B., Hajjar, J. 2014c).

In order to assess and monitor the health condition of infrastructure through finite element analysis, computational models including up-to-date geometry, material and damage information should be generated. The structural modelling procedure developed for this study aims to enable the automatic generation of computational modelling from collected 3D raw point cloud data, derived semantic/information models, or a combination of both. Macro-level computational models using beam-type element will be generated to enable efficient linear and nonlinear analysis for characterizing the shortcomings and identifying key components of infrastructures. In order to assess the health conditions more accurately, high-fidelity continuum models with nonlinear material and geometric properties are also created. The resulting computational models are correlated with observed damage information. These computational models coupled with high-precision nonlinear finite element analysis will provide information on up-to-date conditions and behavior of infrastructure systems with possibilities for documenting damage information, damage propagation, remaining life, and related assessments.

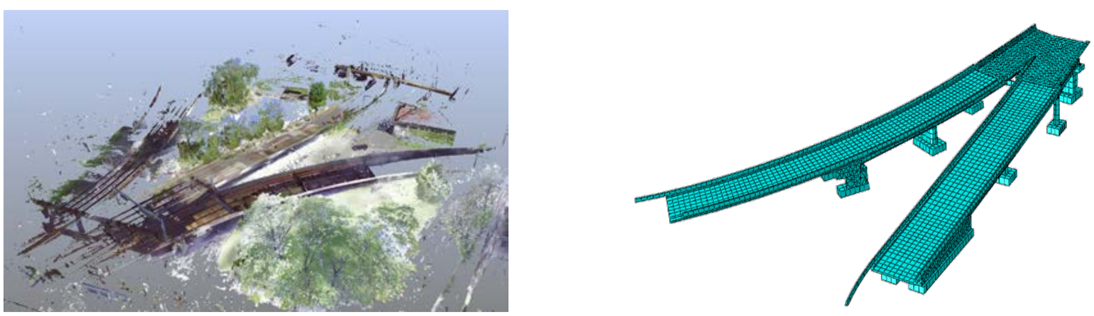

Figure 3: Automated generation of finite element model of damaged steel girder bridge system

The final theme in this project is immersive and information-rich visualization with interaction. Structural models mainly contain mesh details (mesh type, nodes etc.) that represent each bridge element. Prior to that, semantic models only contain information on element types, constraints, topological information etc. This information still needs to be integrated with inspection and maintenance related data to have a complete model that can help with overall assessment. For buildings, building information modeling supports integrated visualization and analysis of multi-disciplinary building data that can improve decision making. Building on the concepts within BIM, in this work a model is being created that integrates information related to semantic modeling, visual inspection, and structural modeling and analysis. At the same time, visualizing such an information-rich model in virtual reality (VR) environments provides a spatially immersive experience to the inspectors, providing benefits, such as: (i) improved situational awareness allowing inspectors to rapidly orient themselves with respect to the structure; (ii) an ability to conduct virtual inspections in real time as well as at a later time, supported by context-sensitive information displays; (iii) an ability to track defect deterioration and stress propagation by superimposing and comparing models over time; (iv) enhanced training and evaluation of inspectors by revisiting and rechecking results from the permanent 3D record of the structure. In this work, current bridge data standards have been extended to represent relevant inspection, modeling and analysis information (Kasireddy and Akinci 2015a); and as-is bridge information models are being generated to integrate inspection related information with those models (Kasireddy and Akinci 2015b). More recently, through empirical user studies, we also evaluated how different VR environments support typical operator tasks on a virtual site (Kasireddy et al. 2016).

Figure 4: Virtual inspection tool

This paper will focus on two parts of the project: damage detection and structural modelling. In the first part, an overview on a set of detection strategies for identifying both element and surface damage are proposed. The proposed methods are used to process the 3D texture mapping point cloud collected from the Bowker Overpass in Boston, Massachusetts to detect surface damage. The second part proposes two mesh generation strategies for generating high-quality volumetric finite element meshes from collected 3D point clouds. The proposed strategies are validated through generating computational models of experimental specimens and comparing analysis results to the experimental data. In order to show the effectiveness of proposed strategies, the algorithms are tested on a real point cloud collected from the Bowker Overpass.

An Overview of the Developed Surface Damage Detection Strategies for Texture-Mapped Point Clouds

In the past two decades, researchers developed several methodologies for using laser-scanning technology for both monitoring structures and detecting damage. Most of the current methodologies used for structural monitoring consist of measuring high-accuracy displacements, strains, pressures, or related quantities of a small number of points or collecting information with visual inspection carried out by expert personnel (Chang et al. 2003). In this part of the paper, the focus is mainly on the surface damage detection capabilities of the laser scanning technology that captures 3D point clouds with color information (Gulder and Hajjar 2013, 2014a, 2014b, 2015; Guldur et al. 2015). Since the texture-mapped point cloud-capturing laser scanning is a fairly new technology, its usage for damage detection has not been investigated extensively. Anil et al. (2015) used point clouds to generate Building Information Model (BIM) of reinforced concrete walls and performed BIM–based earthquake damage assessment. Li et al. (2008) used the LiDAR data and imagery for performing post-earthquake assessment, in order to determine the building damage degree. General overview of remote sensing and GIS applications for damage assessment are discussed in Yamazaki (2001).

Laser-based structural sensing and surface damage detection strategies have been discussed extensively in Guldur and Hajjar (2014c). A brief summary of the developed strategies and several field damage detection examples are presented.
First, a surface-normal based damage detection method that only uses the 3D coordinate information for locating rupture, spalling, delaminations is developed. This method is improved by using intensity values along with the 3D point information for locating small deformations such as cracks, corrosion (Fig. 5 and Table 1). A graph-based damage detection method for detecting alignment issues and points of discontinuity has also been developed in this work. This method is an extension of the graph-based object detection method that generates skeletons from cross-section cuts of a voxelized cluster, where a represents voxel is a single sample or data point on a regularly spaced, three-dimensional grid, through extracting skeleton of an object in order to detect common structural members. The deviations from the predicted object alignments are used for extracting problematic locations on structures (Fig. 6). A method is also introduced that converts cross-section voxel representation automatically into a polygon for computing the changes in the cross-section through area calculation and determining the total volume change on the investigated member (Fig. 7).

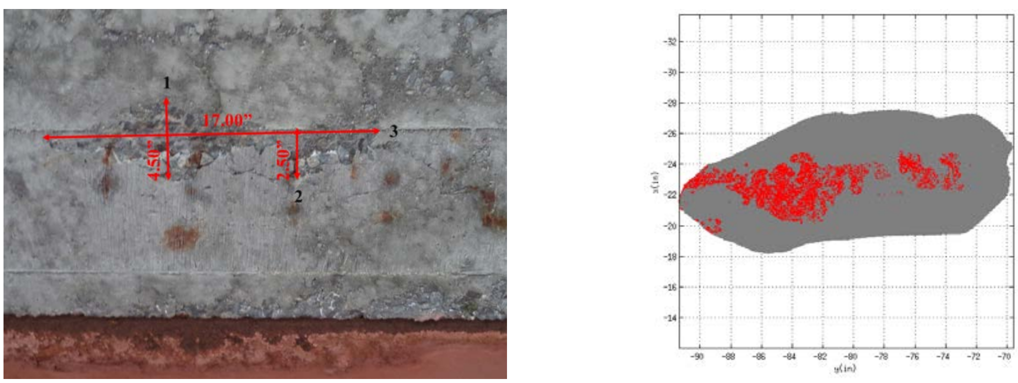

(a) (b)

Figure 5: (a) Image of the processed portion of the Bowker Overpass for spalling detection and (b) result of the surface normal-based damage detection algorithm.

Table 1: Comparison between the field measurements and computed dimensions for the spalling shown in Figure 5.

Defect ID	**Measurement Number**	**Field Measurement (in)**	**Computed Dimension (in)**	**Error (%)**
CS1	**1**	4.50	4.36	3.11
	2	17.00	17.85	−5.00
	3	2.50	2.18	12.80

Detected defects are automatically clustered and a mesh grid-based defect area and volume extraction method is developed in order to obtain quantifiable defect outputs for further investigation. For smaller defects such as cracks, an additional methodology is proposed for automated crack length and width extraction (Fig. 8 and Table 2). An artificial neural network classifier is used for extracting true positives from detected crack clusters from point clouds (Guldur and Hajjar 2014; Guldur et al. 2015).

Finally, a decision-making system based on detected defects for automated condition rating assignment to investigated items of the structure. Several condition rating systems for bridges are investigated and the portions that are required for automated condition rating assignment are determined (Guldur and Hajjar 2014, Guldur and Hajjar 2015).

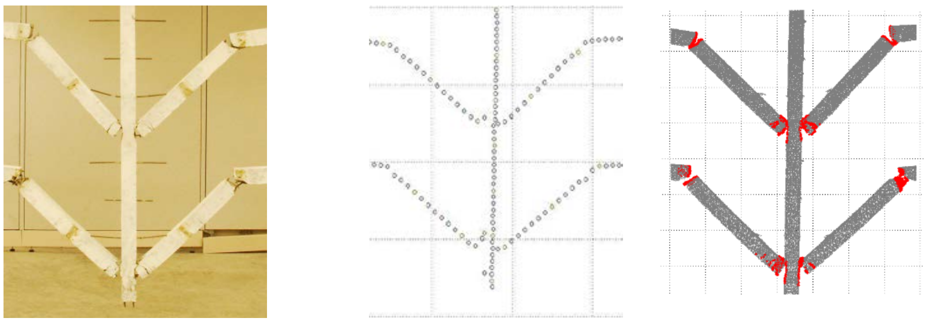

(a) (b) (c)

Figure 6: (a) Image of a portion of the concrete testing frame, (b) skeleton of the concrete testing frame and (c) defect detection results shown on corresponding portion of the point cloud.

(a) (b)

Figure 7: (a) Model drawing of a C-section and (b) damaged cross-section representation extracted from laser scan.

(a) (b)

Figure 8: (a) Image of the processed portion of the Bowker Overpass for crack detection and (b) result of the crack detection algorithms.

Table 2: Comparison between the field measurements and computed crack dimensions for the crack shown in Figure 9.

Defect ID	Measurement Points	Field Measurement (in)	Computed Dimension (in)	Error (%)
Crack 1	**1-2**	6.75	6.74	0.15
	2-3	8.25	8.28	-0.36

Overview of Mesh Generation Strategy for Laser Point Clouds

Generating finite element models directly from laser point clouds and images is a key component of this research, since the purpose is to enable integrated structural assessment by comparing the nonlinear analysis results with the damage detected automatically from the collected laser scans and images.

Recently, several efforts have been made in the field of generating finite element models from laser scanning. Hinks et al. (2013) developed an algorithm for automatically generating a finite element models of a masonry building façade from a laser point cloud directly through a voxelization method. Finite element analysis was conducted on the generated model and results were shown to be convergent. However, this method can only be applied to planar models. For generating 3D computational models, Conde-Carnero et al. (2015) proposed a method for generating finite element models of bridges using data collected by laser scanning. A geometric CAD model was created manually first and then converted to a finite element model. This method thus requires extensive human interaction. An automatic method for generating a 3D finite element model of historic masonry structures from laser point clouds was developed by Castellazzi et al. (2015). Jagged finite element meshes are generated through a voxelization process and then are smoothed using a Laplacian smoothing algorithm. However, the resulting finite element meshes always overestimate the actual size of structure based on the size of the voxels, making this approach inapplicable for modelling thin members. In this paper, a method combining voxelization and grid-based mesh generation is proposed to generate accurate 3D finite element meshes directly from point clouds. The generated models are validated against experimental specimens.

Mesh Generation Methods

One important step of creating finite element model is to generate high-quality volumetric finite element meshes. To achieve better simulation accuracy, hexahedral elements are always preferred in finite element analysis due to their advantages for interpolation. Compared to tetrahedral elements, to achieve the same accuracy, using hexahedral elements can reduce computational costs.

Many efforts have been made for developing algorithms for generating high-quality structured hexahedral meshes automatically based on an arbitrary geometry. Existing all-hexahedral mesh generation methods can be classified into four categories: Mapping Method (Blacker 1996), Tetrahedron Transforming Method (Li et al. 1995), Advancing Front Method (Owen et al. 2000 and Staten et al. 1998), and Grid-based Method (Schneiders 1996 and Lee et al. 1999). The Mapping Method produces high-quality meshes in regular geometries but requires user interaction for decomposition when encountering complex geometries. Several researchers in the CUBIT project (Cubit meshing generation toolkit) focus on automatically decomposing complex geometries into simple primitives that can be meshed using mapping method. However, none of those algorithms are robust enough to decompose arbitrary geometry. The second method, the Tetrahedron Transforming Method, starts with producing all-tetrahedral meshes first and then decomposes each tetrahedron into four hexahedrons. However, the quality of resulting all-hexahedral meshes is often poor. The next method, the Advancing Front Method forms mesh of all hexahedral elements on the boundary surface and then generates hexahedrons layer by layer from the boundary to the center of the volume of interest. This method usually produces high-quality meshes at the boundary but poor-quality interior meshes. Finally, the Grid-based Method starts with generating interior hexahedral meshes and leaving some space between the interior mesh and object boundary where a new layer of hexahedral meshes will be generated later. Although the resulting boundary meshes are probably of poor-quality, this method has capability of being highly automated, controlling mesh density and generating a high-quality interior mesh. As such, the grid-based mesh generation is used in this paper.

In the field of grid-based hexahedral mesh generation, significant research has been done on controlling mesh density and improving mesh quality. Schneiders (1996) proposed hexahedral refinement templates for local hexahedral mesh refinement. Zhang et al. (2007) proposed algorithms for automatic determination of both refinement region and refinement level based on geometric curvature and local thickness. Ito (2009) proposed additional refinement templates so that local refinement region can be confined precisely. Staten et al. (2008), Daniels et al. (2009) and Shepherd et al. (2010) make contributions on local quadrilateral and hexahedral mesh coarsening. Since the resulting boundary meshes of the grid-based method are of poorer quality, Zhang et al. (2010) and Sun et al. (2012) proposed approaches for improving the quality of boundary meshes.

Grid-based Mesh Generation

Introduced by Schneiders (1996), the grid-based mesh generation algorithm works in two steps: (1) fill the interior volume with regular meshes; (2) mesh the boundary region with a new layer of finite elements. This method is capable of generating both quadrilateral meshes on a 2D object and hexahedral meshes on a 3D object. The advantages of this method is the capability of generating all quadrilateral/hexahedral meshes automatically, which is an important feature when the region needs to be re-meshed repeatedly. This method was originally designed for generating finite element meshes on objects described by CAD geometry models. This paper aims to implement this method on geometries that are described by laser point clouds. A 2D example is shown in Fig. 9.

In order to generate a uniform-distributed regular interior mesh, a region of interest is created containing the object and is then divided into uniform grids. The size of the grids is set to the size of mesh for the interior mesh region, because these grids are converted into meshes. Once uniform grids are built, the captured point cloud will be mapped onto these grids. All grids containing points of more than a threshold (set according to the resolution of the point cloud) will be labeled as a *boundary grid*. The volume/area enclosed by the boundary grid will be labeled as an *interior grid*, and all the rest will be marked as an *exterior grid*. A uniformly-distributed interior mesh can be generated on the basis of the interior grids by creating nodes at each corner of the grids as well as defining the edges, faces and elements connecting the nodes.

The gap between the interior mesh and the object boundary is filled with a new layer of quadrilateral meshes through the following procedure:

(1) All boundary nodes and edges need to be identified. All edges that are shared less than two elements are labelled as *boundary edges* and all nodes that are shared by less than four elements are labelled as *boundary nodes*.

(2) The normal vector ($\overrightarrow{n_e}$) of each boundary edge is computed and set to be pointing outward from its associated element. The project vector ($\vec{n}$) of each boundary node is then calculated by taking the average of the normal vectors of the connecting boundary edges as show in Eq. 1:

$$\overrightarrow{n_i} = \frac{1}{k}\sum_{j=1}^{k} \vec{n}_{ej} \tag{1}$$

(3) The corresponding point of each boundary node is identified by the intersection points of the projection vector and object boundary. As shown in Fig. 9(e), points 3 and 4 are the corresponding points of points 1 and 2.

(4) A new layer of quadrilateral meshes are formed by connecting a pair of boundary nodes and their corresponding points as shown in Fig. 9 (e).

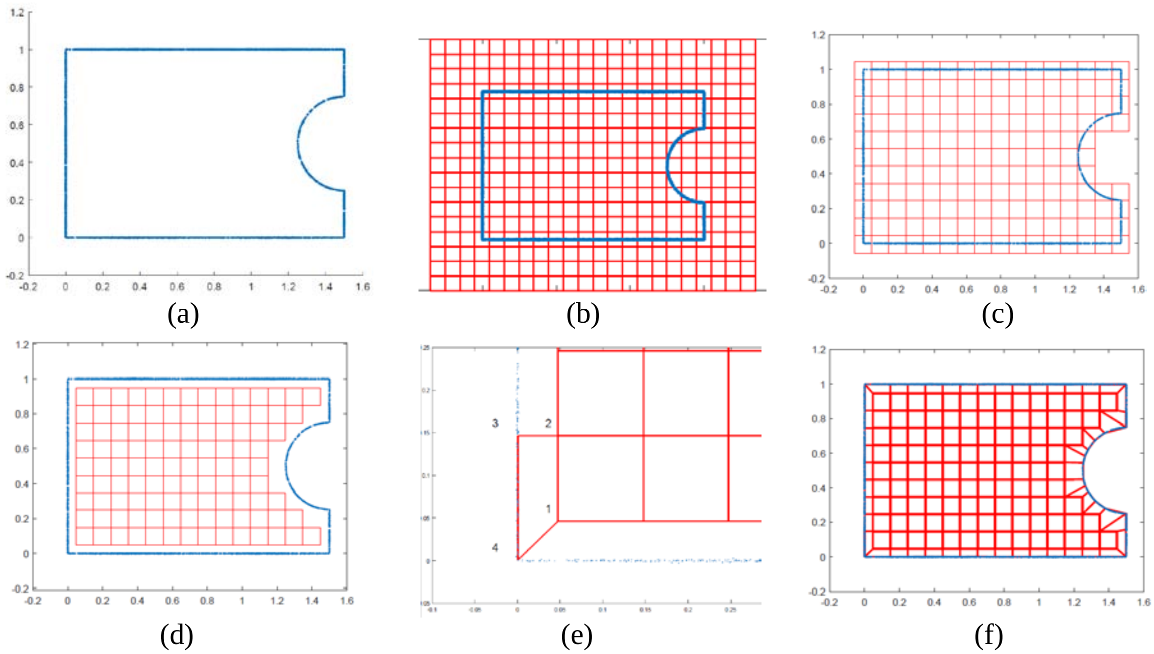

Figure 9: Steps of 2D grid-based method: (a) Synthetic point cloud (reflected in blue line); (b) Voxelize the region of interest; (c) Convert active voxels to meshes; (d) Create internal meshes; (e) Fill the gap with a new layer of quadrilateral meshes; (f) Final all-quadrilateral meshes.

Cross section extrusion

Although Grid-based Mesh Generation is capable of generating 3D hexahedral elements, it is not preferred because of its high computational cost and potential for lower mesh quality. If an extrudable 3D geometry model (a model that has a prismatic cross section and unique extrusion direction) needs to be meshed, a better approach is to generate a 2D quadrilateral mesh for its cross-section first and then extrude the 2D quadrilateral mesh to a 3D hexahedral meshes. Thus, before implementing the grid-based method, the model will be checked automatically to determine if a consistent cross section can be found along a specific direction. If so, the cross section information, extrusion direction and extrusion length are extracted. A 3D volumetric mesh is then generated using the extrusion-based method. If no consistent cross section can be found on the geometry, then it is meshed in a 3D grid-based method.

In order to check the extrusion information, the surface normal of each point representing its local feature is first estimated. For a specific point, a plane is fit to a point group consisting of this point and its k-nearest neighbor points, where k is determined based on the mesh density. The normal vector of this fitted plane is defined as the surface normal of this point. After all surface normals are estimated, they are used for principle component analysis (PCA). If the point cloud represents an extrudable model exactly without any extraneous points, the third principle component should be the extrusion direction and perpendicular to all surface normals. In the case of the existence of extraneous points, the angles between extrusion direction and each surface normal are calculated. Any points with an angle less than a user-defined angle threshold (which is taken as 85° in this paper) will be removed. All steps starting from the surface normal estimation will be performed on the remaining points. This process is repeated until no points are left to be removed. If the remaining point cloud contains points more than 80% of original point cloud, the model will be identified as an extrudable model. Otherwise, the model is identified as non-extrudable and the 3D grid-base method is used.

Local Refinement

Since computational resources are limited, meshes need to be made as coarse as possible. However, in terms of improving the accuracy of finite element analysis, a finer mesh is required in areas of high strain gradients. A method has been developed to locally refine the meshes automatically, especially on the locations with high geometric curvature and large deformation. An octree-based method is used in this work to achieve the local refinement with the following requirements: (1) all resultant meshes are still quadrilateral/hexahedral meshes; (2) the meshes have no hanging nodes; (3) the resultant meshes have preferred aspect ratio (<3); (4) the geometry of object can be captured with an accepted accuracy. The template used for refining both quadrilateral and hexahedral meshes are proposed by Scheneiders et al. (1996).

The exterior layer of meshes from grid-based method is not always of good-quality, and the refinement process makes them worse or potentially unacceptable for finite element analysis. As such, the local refinement is executed right before creating the interior meshes, as shown in Fig.10. After the local refinement, all nodes and elements located outside or on the object boundary will be deleted to form an interior mesh. The exterior layer of mesh will be generated through the projection method as show in Fig. 9(e).

Mesh Quality

High quality meshes are crucial for finite element analysis both for simulation accuracy and computational efficiency. Two quality metrics are used in this work to ensure the generated meshes are suitable for finite element analysis: Aspect Ratio and Scaled Jacobian (Knupp, 2000). The Aspect Ratio of an element is calculated by Eq. 2:

$$AR = {}^{L_{max}}/_{L_{min}} \tag{2}$$

where L_{max} is the length of longest edge and L_{min} is the length of shortest edge. An AR ≤ 5 is preferred in finite element analysis.

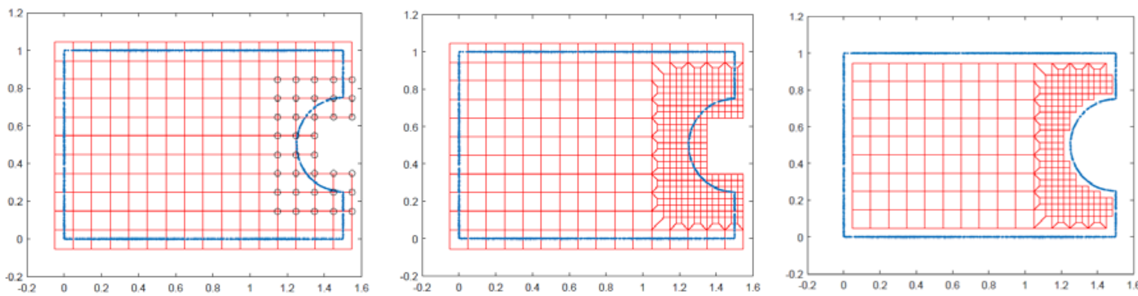

(a) (b) (c)

Figure 10: Steps of local refinement: (a) Convert active voxels to meshes and define the region of refinement; (b) Locally refine meshes with good connectivity; (c) Create internal mesh

The other metric, Scaled Jacobian, refers to the determinant of the normalized Jacobian matrix and is defined for each node. The Jacobian matrix for a node is calculated by Eq. 3:

$$J_m = \begin{bmatrix} x_{m,1} - x_m & x_{m,2} - x_m & x_{m,3} - x_m \\ y_{m,1} - y_m & y_{m,2} - y_m & y_{m,3} - y_m \\ z_{m,1} - z_m & z_{m,2} - z_m & z_{m,3} - z_m \end{bmatrix} \tag{3}$$

where $x_{m,i}$ is the x coordinate of i-th neighbor node of node m in an element. If each column vector in the Jacobian matrix is normalized, then the result is called a normalized Jacobian matrix. Since there are eight scaled Jacobians for one element, the minimum (worst) one is selected as a measure of the quality of the element. The minimum requirement is scaled Jacobian ≥ 0 and a scaled Jacobian ≥ 0.5 is preferred in finite element analysis.

Validation and Testing

In order to ensure the resultant volumetric finite element mesh yields a good simulation result, this mesh generation algorithm is validated against experimental results. Since the experimental specimens were no longer available, a CAD model was created for each experimental specimen and then a point cloud was generated through a virtual-scanning process. This process puts multiple laser scanners around the model and scans all surfaces virtually. The point clouds are then captured from each scanner and registered through using an Iterative Closest Point (ICP) algorithm. The noise parameter of the virtual laser scanner is set to be consistent with noise produced by a Faro Focus laser scanner, which has been used for collecting real data on this project using a terrestrial laser scanner. The point clouds of the first two experimental specimens discussed here are downsampled to a resolution of 0.1 cm.

Error quantities in the simulations are computed to evaluate the quality of the simulation. In this work, the errors are determined by computing the normalized energy difference as shown in Eq. 4, where E_{EX} refers to the energy of the experiment results and E_{FE} refers to the energy of the simulation results. The energy is calculated as the area under the monotonic force-displacement curve for key force and displacement quantities in the simulation:

$$Error = \frac{E_{EX} - E_{FE}}{E_{EX}} \tag{4}$$

In addition, the mesh generation algorithm is tested on both a synthetic point cloud from a shear tab connection and real point cloud from a portion of the Bowker Overpass. The synthetic point cloud of the shear tab connection model is generated by the same virtual scanning process and downsampled to a resolution of 1 cm. The real point cloud was collected by a FARO Focus 3D laser scanner and texture mapped through images collected by high-resolution cameras.

Circumferentially Notched Tension Specimen

In the first validation example, a one-eighth symmetric model of an original model was used with appropriate symmetrical boundary conditions to simulate an experimental circumferentially notched tension (CNT) specimen tested by (Myers et al. 2009). The one-eighth model has been validated against a full model of the specimen through comparing both force-displacement curves and stress contours. The finite element mesh for this CNT model is generated through the 3D grid-based method as show in Fig. 11. A36 steel is used for these CNT specimens and the plasticity and fracture models have been validated by Saykin et al. (2014). The model is analyzed in ABAQUS/Explicit using a mesh from grid-based method with first-order interpolation displacement shape functions and reduced integration.

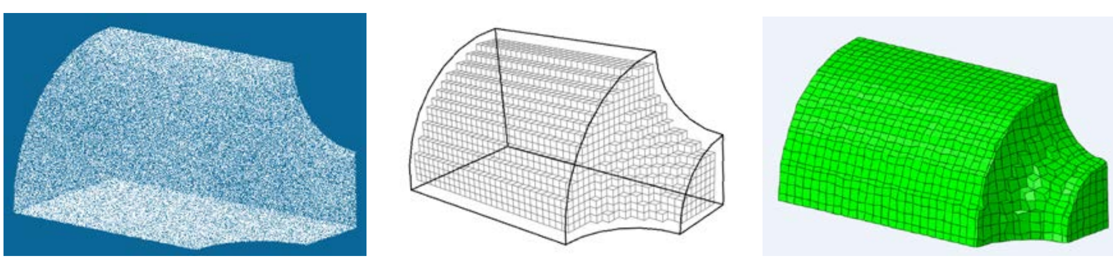

Figure 11: 3D grid-based method for meshing CNT

The generated meshes have a maximum aspect ratio of 5.39 and minimum scaled Jacobian of 0.202. The resulting mesh quality metrics are shown in Fig. 12, with the large majority of values confirming the accuracy of the mesh.

The resultant force-displacement curve shown in Fig. 13 is able to capture the elastic and hardening behavior as well as the fracture initiation of the specimen in experiment. Also, the softening behavior and fracture propagation are captured with an acceptable accuracy. The overall energy error in the simulation for the plot shown is 9.53%, and is much smaller than this value prior to the fracture occurring in the simulation.

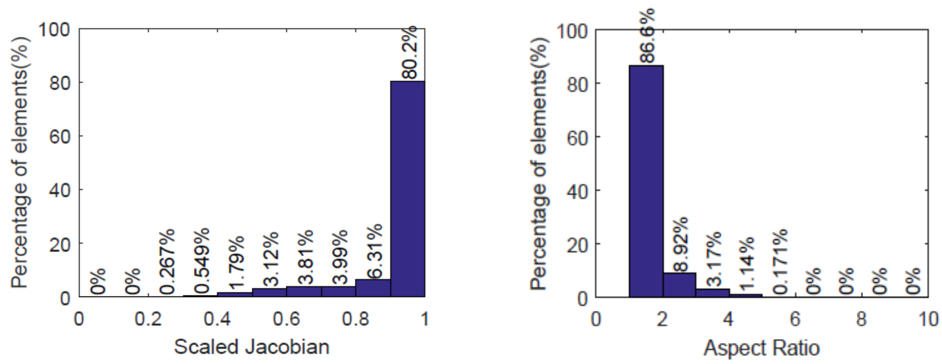

(a) (b)

Figure 12: Mesh quality metrics of CNT meshes: (a) Scaled Jacobian; (b) Aspect Ratio

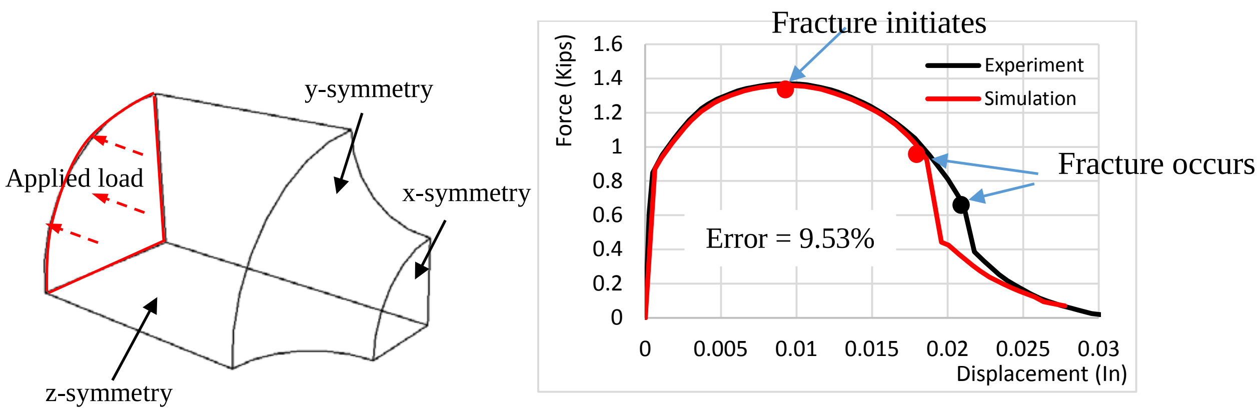

Figure 13: Applied boundary condition and resulting force-displacement curve compared to experimental results of Myers et al. 2009

Tensile Plate Specimens

Another experimental specimen being used for the validation is a tensile plate specimen tested by (Kanvinde et al. 2004). A one-quarter model is used in this analysis with symmetric boundary conditions applied at appropriate locations. A572 Grade 50 steel is used for this specimen, and the constitutive relations and fracture model used are those validated by Saykin et al. (2014).

Even though a consistent cross section could be extracted for this model, a 3D grid-based method is used here due to its short extrusion length as shown in Fig. 14. At user-defined region, the mesh is refined automatically using a 3D refinement template in order to improve the accuracy of the finite element analysis.

The generated meshes for the tensile plate specimen have a maximum aspect ratio of 7.44 and a minimum scaled Jacobian of 0.143. Details of the mesh quality metrics are shown in Fig. 15. A majority of the mesh has an aspect ratio of between 2.0 and 3.0 because the size of the elements along the thickness direction is set to be half of the size along the other two directions.

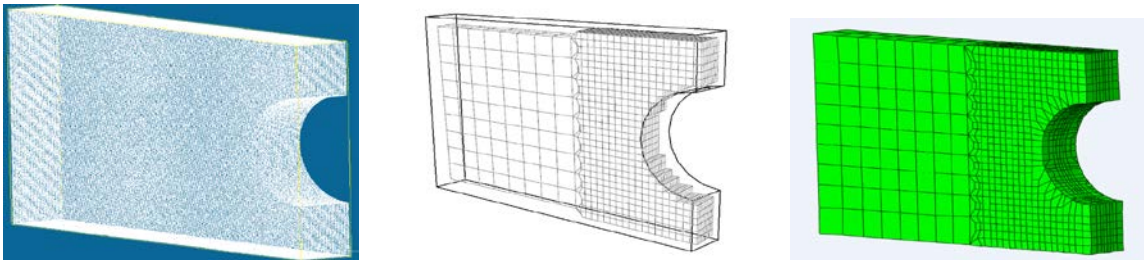

Figure 14: 3D grid-based method for meshing tensile plate specimen

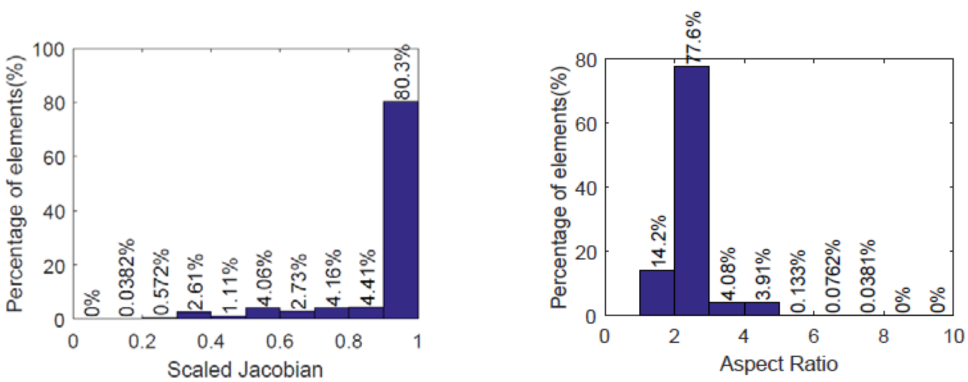

(a) (b)

Figure 15: Mesh quality metrics of meshes in tensile plate: (a) Scaled Jacobian; (b) Aspect Ratio

The resultant force-displacement curve shown in Fig. 16 is able to capture the elastic and hardening behavior of the experiment. Also, the softening behavior, fracture initiation and fracture propagation are captured with good accuracy. The energy error within the simulation is computed to be 7.00% for the plot shown.

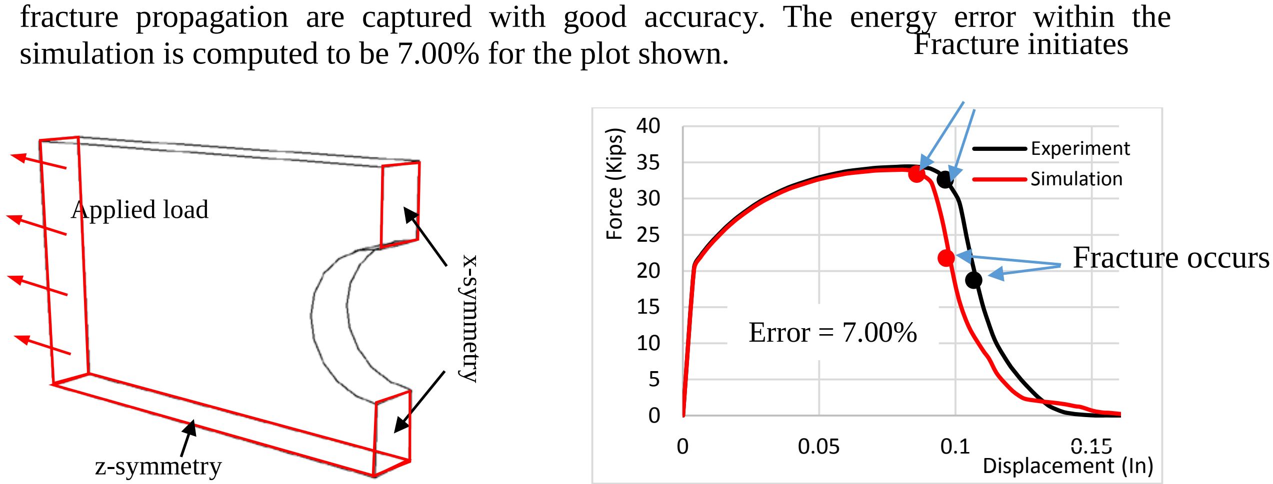

Figure 16: Applied boundary condition and resulting force-displacement curve compared to experimental results of (Kanvinde et al. 2004).

Shear Tab Connection

In order to test the capability of the automated meshing scheme on more complex structural components, the mesh generation algorithm is tested on a shear tab connection experiment tested by (Birkemoe et al. 1978). For the shear tab model, different parts of the assembly (e.g., the beam, column, angles, bolts, nuts) need to modelled separately because they have different material properties. The beam, column and angles are meshed through automatically meshing and extruding a 2D quadrilateral mesh of cross section because a consistent cross section is detected in these components. In order to detect the size of the bolt while only the bolt head is visible, a synthetic point cloud of a bolt head is generated for each available bolt size in the industry and is stored in a library. The synthetic point cloud in the library that then matches with the actual point cloud with minimum error is selected as the bolt size for generating the bolt meshes. Bolts point clouds are not detected to have a consistent cross section and are thus meshed by the 3D grid-based method. Once the finite element meshes of all parts are generated, they are automatically mapped to the original position and assembled. Since all parts are meshed independently, mesh intersections often arise. As such, intersected meshes are detected and replaced by a new layer of mesh as show in Fig. 17. In addition, user defined contact interaction and constraints are assigned to all the surface contact points resulting from the assembly step automatically. Fig. 18 shows the final assembled finite element mesh generated from the laser point cloud.

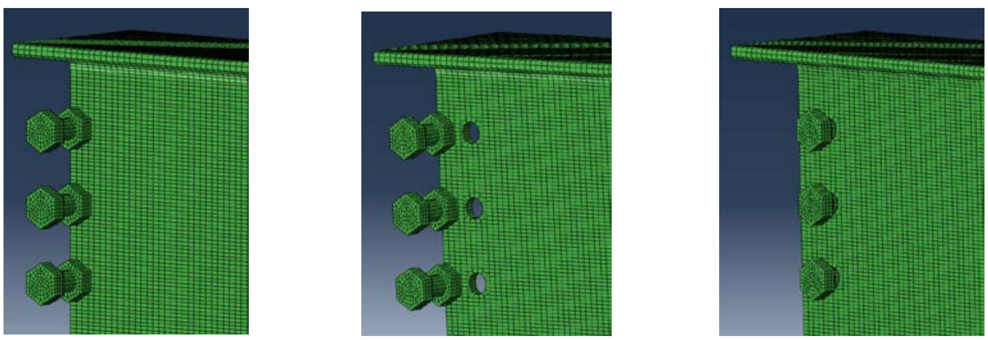

(a) (b) (c)

Figure 17: Mesh assembly: (a) independently generated meshes of beam and bolts; (b) delete intersected mesh and generate a new layer of mesh; (c) assemble meshes

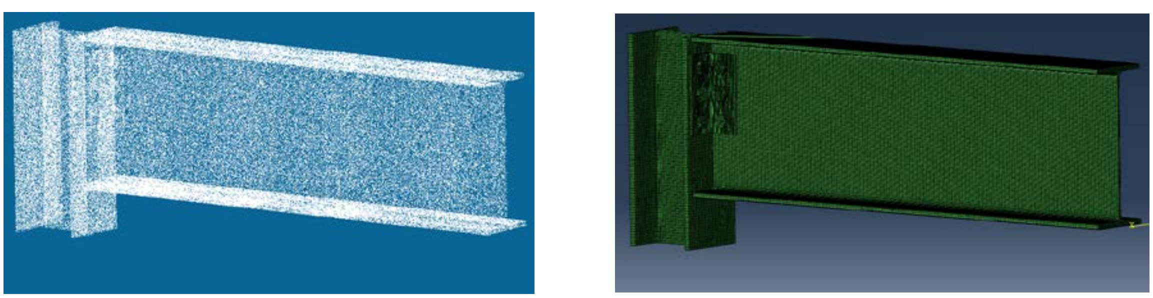

Figure 18: Automated mesh generation of shear tab connection

In the shear tab connection model, the generated meshes have a minimum scaled Jacobian of and a maximum aspect ratio of 9.3. As shown in Fig. 19, the majority of the meshes have an aspect ratio of 2.0 to 3.0 because the size of the mesh along the extrusion direction is set to be twice that along the other two directions. Most of the parts of the mesh that have poorer quality are generated when generating a new layer of mesh in the mesh assembly step, thus located around the region of the bolt holes. in the future, additional efforts will be made to generate more accurate meshes in the assembly step.

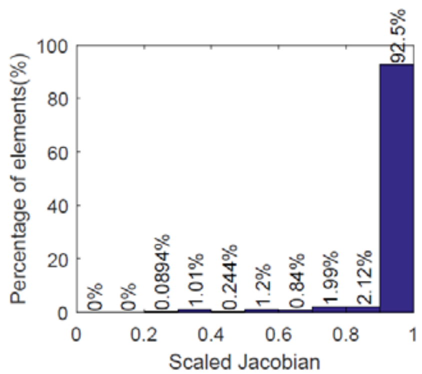

(a)

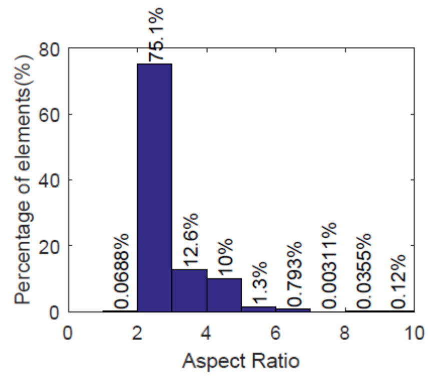

(b)

Figure 19: Mesh quality metrics of meshes in shear tab connection:
(a) Scaled Jacobian; (b) Aspect Ratio

In the experiment, the materials used are G40.21 Grade 44W steel and ASTM A325 bolts. In the finite element analysis, the constitutive law and fracture parameters of the steel components are used as put forward and calibrated by Saykin et al. (2014). The applied load and boundary conditions are shown in Fig. 20.

The force-displacement curve in Fig. 20 shows the two curves share a similar shape but there is an offset between them. A small gap in the bolt hole between the bolt shank and hole requires the beam to slip into bearing prior to engaging. As a result, sliding happens and leads to larger displacement in finite element analysis. Future efforts will be made to automatically detect and fill all gaps to eliminate these errors.

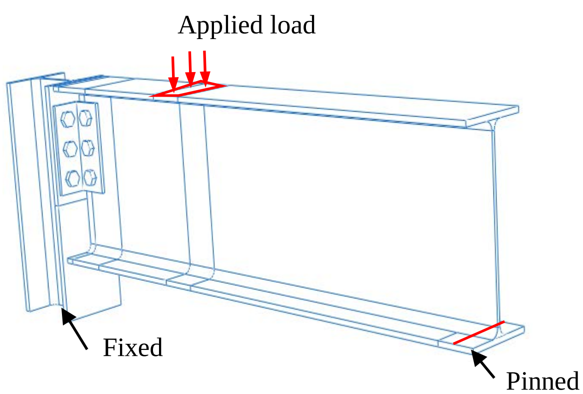

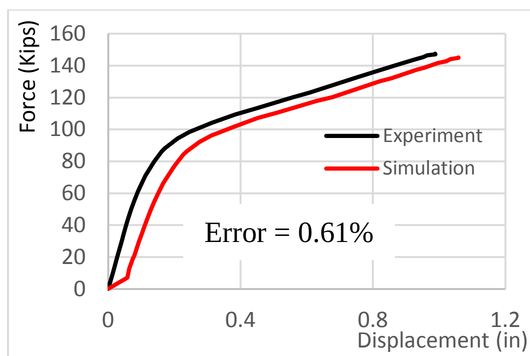

Figure 20: Applied boundary condition and resulting force-displacement curve compared to experimental results of (Birkemoe et al. 1978).

Bowker Overpass

A portion of the point cloud collected from real scans using a terrestrial laser scanner is used for testing the mesh generation algorithm as well. A complete series of scans was taken of the Bowker overpass bridge, a steel girder bridge with composite concrete deck. The terrestrial laser scanner is used as a first step for creating the meshes of this complex bridge due to the enhanced resolution. These algorithms are then being extended to address the coarser resolution provided by UAV scans. Because the data is texture-mapped from the use of cameras, the color information is used to segment the point cloud into two parts:

concrete deck and steel I beam. The noise in point cloud is removed by fitting planes to each planar portions of the point cloud using a RANSAC algorithm (Schnabel et al. 2007). The same methodology as used in meshing the shear tab connection is applied to create the finite element meshes for this structural system (shown in Fig. 21).

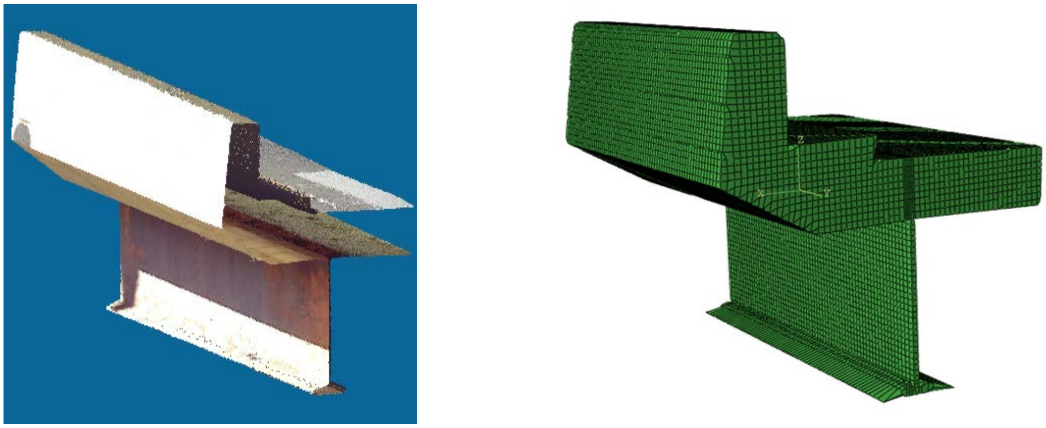

Figure 21: Automated mesh generation of a portion of Bowker Overpass

Conclusions

This paper summarizes research on developing algorithms for use in using unmanned aerial vehicles for automated creation of in situ geometries and damage detection in civil infrastructure. The paper focuses on the proposed strategy for combining voxelization and grid-based methods to directly convert texture-mapped laser point cloud data into volumetric all-hexahedral finite element meshes. Each captured laser point cloud is processed first to check automatically if a consistent cross section and extrusion direction can be found. If not, a 3D grid-based mesh generation method is used to generate all-hexahedral meshes. However, for those point clouds from which a consistent cross section and unique extrusion direction can be found, all quadrilateral meshes for the cross section are generated through a 2D grid-based method and then extruded to form 3D volumetric hexahedral meshes. This method is capable of generating meshes with high quality as well as reducing computational cost. Regions with high geometric curvature are automatically refined in order to improve simulation accuracy. The resulting meshes are of high quality and can be imported directly into commercial software such as ABAQUS/Explicit for conducting fully nonlinear analysis including damage propagation and fracture, which are shown to compare to tests with excellent accuracy.

Future work will include: (1) extension of all algorithms to address lower resolution scans conducted by UAVs; (2) automatic object-oriented classification of point clouds in order to process large datasets; (3) automatic identification and assignment of stochastic material properties and boundary conditions from texture-mapped laser data; (4) automatic coarsening of hexahedral meshes; (5) automated feedback to the UAV based on stochastic analysis results to highlight regions where additional scans may be needed.

Acknowledgements

This material is based upon work supported by National Science Foundation under Grant No. IIS-1328816 and Northeastern University. This work used the Extreme Science and Engineering Discovery Environment (XSEDE), which is supported by National Science

Foundation Grant No. OCI-1053575. Any opinions, findings and conclusions in this material are those of the authors and do not necessarily reflect the views of National Science Foundation. The authors thank Julieta Moradei, William Huang, Ramsey Barghout, Michael MacNeil, Kyle Coleman, Michael Clifford of DGT Survey Group, Faro Technologies, and the Massachusetts Department of Transportation for their assistance with this research.

References

Anil, E. B., Akinci, B., Kurc, O., Garrett, J. H. (2015). “Building-information-modeling–based earthquake damage assessment for reinforced concrete walls,” *Journal of Computing in Civil Engineering*, Paper No. 04015076.

Birkemoe, P. C., Gilmore, M. I. (1978). “Behavior of bearing critical double-angle beam connections,” *Engineering Journal*, 4(15), 109-115.

Blacker, T. (1996). The Cooper toll, *Proceedings of the Fifth International Meshing Roundtable*, pp: 13-30.

Castellazzi, G., Maria D’Altri, A., Bitelli, G., Selvaggi, Ilenia, Lamebertini, A. (2015). “Form laser scanning to finite element analysis of complex building by using a semi-automatic procedure,” *Sensors*, 15(8), 18360-18380.

Chang, P. C., Flatau, A., Liu, S. (2003). “Review paper: health monitoring of civil infrastructure.” *Structural Health Monitoring*, 2(3), 257-267.

CUBIT, *Sandia National Laboratories*. Available from: https://cubit.sandia.gov/

Conde-Carnero, B., Riveiro, B., Arias, P., Caamano, J. (2015). “Exploitation of geometric data provided by laser scanning to create FEM structural models of bridges,” *Journal of Performance of Constructed Facilities*, Paper No. 04015053.

Daniels II, J., Silva, C., Cohen, E. (2009). “Localized quadrilateral coarsening,” *Eurographics Symposium on Geometry Processing,* 28,

Guldur, B., Hajjar, J. F. (2013). “Laser-based automatic cross-sectional change detection for steel frames,” Proceedings of the 9th International Workshop on Structural Health Monitoring 2013, Stanford, California, September 10-12, 2013, Stanford University, Stanford, California.

Guldur, B., Hajjar, J. F. (2014a). “Damage detection on structures using texture mapped laser point clouds,” Proceedings of the ASCE/SEI Structures Congress 2014, Boston, Massachusetts, April 3-5, 2014.

Guldur, B., Hajjar, J. F. (2014b). “Automated damage assessment from 3-d laser scans,” Proceedings of the 2014 Istanbul Bridge Conference, Istanbul, Turkey, August 11-13, 2014, Middle East Technical University, Ankara, Turkey.

Guldur, B., Hajjar, J. (2014c). “Laser-based structural sensing and surface damage assessment,” Report No. NEU-CEE-2014-03, Department of Civil and Environmental Engineering, Northeastern University, Boston, Massachusetts, August, 375 pp.

Guldur, B., Yan, Y., Hajjar, J. F. (2015). “Condition assessment of bridges using terrestrial laser scanners,” Proceedings of the 2015 SEI Structures Congress, Portland, Oregon, April 23-25, 2015, ASCE, Reston, Virginia.

Guldur, B., Hajjar, J. F. (2015). “Laser-based condition assessment assistant for bridges,” Proceedings of the 2015 International Symposium on Non-Destructive Testing in Civil Engineering, Berlin, Germany, September 15-17, 2015.

Hinks, T., Carr, H., Linh, T., Laefer, D. (2013). “Point cloud data conversion into solid models via point-based voxelization,” *Journal of Surveying Engineering*, 72-83

Ito, Y., Shih, A., Soni, B. (2009). “Octree-based reasonable-quality hexahedral mesh generation using a new set of refinement templates,” *International Journal of Numerical Methods in Engineering*, 77(13), 1803-1833.

Kanvinde, A. M., Deierlein, G. G. (2004). “Micromechanical simulation of earthquake-induced fracture in steel structures, *Report #145*, The John A. Blume Earthquake Engineering Center, Stanford, California.

Kasireddy, V., Akinci, B. (2015a). “Towards the integration of inspection data with bridge information models to support visual condition assessment,” *Computing in Civil Engineering*, 644-651.

Kasireddy, V., Akinci, B. (2015b). “Challenges in generation of as-is bridge information model: a case study,” *Proceedings of the International Symposium on Automation and Robotics in Construction*, 32, 297-304.

Kasireddy, V., Zou, Z., Akinci, B., Rosenberry, J. (2016). “Evaluation and comparison of different virtual reality environments towards supporting tasks done on a virtual construction site,” *Proceedings of the Construction Research Congress*, in press.
Knupp, P. (2000). “Achieving finite element mesh quality via optimization of Jacobian matrix norm and associated quantities. Part II. A framework for volume mesh optimization and condition number of the Jacobian matrix,” *International Journal for Numerical Methods in Engineering*, 58, 217-241
Lee, Y.K., Yang, D.Y. (1999). “Development of a grid-based mesh generation techniques and its application to remeshing during the finite element simulation of a metal forming process”, *Engineering Computations*, 16, 316-336.
Li, M., Cheng, L., Gong, J., Liu, Y., Chen, Z., Li, F., Chen, G., Chen, D., Song, X. (2008). “Post-earthquake assessment of building damage degree using lidar data and imagery,” *Science in China Series E: Technological Sciences*, 51(2), 133-143.
Li T.S., McKeag, R.M., Armstrong, C.G. (1995). “Hexahedral meshing using midpoint subdivision and integer programming,” *Computer Methods in Applied Mechanics and Engineering*, 124, 171-193.
Li, Z., Huber, D. (2015), “Domain Adaptation for structure recognition in different building styles,” *3D Vision (3DV) 2015*, 206-214.
Myers, A. T., Deierlein, G. G., and Kanvinde, A. (2009). “Testing and Probabilistitic Simulation of Ductile Fracture Initiation in Structural Steel Components and Weldments,” *Report #170*, The John A. Blume Earthquake Engineering Center, Stanford, California.
Owen, S.J., Saigal, S. (2000). “H-Morph: an indirect approach to advancing front hex meshing,” *International Journal of Numerical Method in Engineering*, 1(49), 289-312.
Saykin, V. V., Song, J., Hajjar, J. F. (2014). “A validated approach to modeling collapse of steel structures,” *Report No. NEU-CEE-2014-02*, Department of Civil and Environmental Engineering, Northeastern University, Boston, Massachusetts, August, 538 pp.
Schnabel, R., Wahl, R., Klein, R. (2007). “Efficient RANSAC for point-cloud shape detection,” *Computer Graphics Forum*, 26(2), 214-226
Schneiders, R. (1996). “A grid-based algorithm for the generation of hexahedral element meshes,” *Engineering with Computers*, 12, 168-177
Schneiders, R. (1996). “Refining quadrilateral and hexahedral element meshes,” *Proceedings of the Fifth International Conference on Numerical Grid Generation in Computational Field Simulations*, Mississippi State University, pp. 679-688.
Schneiders, R., Weiler, F. (1996). “Octree-based generation of hexahedral element meshes,” *Proceedings of the 5th International Meshing Roundtable*, Sandia National Laboratories, 205-216
Shepherd, J., Dewey, M., Woodbury, A., Benzley, S., Staten, M., Owen, S. (2010). “Adaptive mesh coarsening for quadrilateral and hexahedral meshes,” *Finite Elements in Analysis and Design*, 46, 17-32
Song, M., Huber, D., (2015). “Automatic Reconvery of Newworks of Thin Structures,” *3D Vision (3DV)* 2015, 37-45.
Staten, M.L., Benzley, S., Scott, M. (2008). “A methodology for quadrilateral finite element mesh coarsening,” *Engineering with Computers*, 24, 241-251
Staten, M.L., Cabann, S.A., Owen, S.J. (1998). “BMSWEEP: Locating interior nodes during sweeping,” Proceedings of the 7th International Meshing Roundtable, Dearborn, MI, pp 7-18.
Sun, L., Zhao, G., Ma, X. (2012). “Adaptive generation and local refinement methods of three-dimensional hexahedral element mesh,” *Finite Elements in Analysis and Design*, 50, 184-200.
Sun, L., Zhao, G., Ma, X. (2012). “Quality improvement methods for hexahedral element meshes adaptively generated using grid-based algorithm,” *International Journal for Numerical Methods in Engineering*, 89, 726-761
Yamazaki, F. (2001). “Applications of remote sensing and GIS for damage assessment,” *Structural Safety and Reliability*, Swets & Zeitlinger, Leiden, the Netherlands.
Yoder, L., and Scherer, S., "Autonomous Exploration for Infrastructure Modeling with a Micro Aerial Vehicle," *Field and Service Robotics*, June, 2015.
Zhang, H., Zhao, G. (2007). “Adaptive hexahedral mesh generation based on local domain curvature and thickness using a modified grid-based method,” *Finite Elements in Analysis and Design*, 43, 691-704
Zhang, J., Singh, S. (2014). “LOAM: Lidar Odometry and Mapping in Real-time”, *Robotics: Science and Systems Conference (RSS)*, July 2014